Channel Error Estimation Algorithm for Multichannel in Azimuth HRWS SAR System Based on a 3-D Deep Learning Scheme

Shaojie Li, Shuangxi Zhang , *Member, IEEE*, Yuchen Lin, Hongtao Zhan, Shuai Wan , *Member, IEEE*, and Shaohui Mei , *Senior Member, IEEE*

Abstract—High-resolution and wide-swath (HRWS) multichannel synthetic aperture radar (SAR) provides extensive imaging coverage, playing a pivotal role in remote sensing applications. Although multichannel in azimuth SAR system has been proposed to deal with the contradiction problem between high resolution and low pulse repetition frequency, the channel errors caused by temperature, timing uncertainty and other factors may result in azimuth ambiguity and defocus. To address this issue, a deep learning-based channel calibration method is proposed in this article, in which multichannel errors can be simultaneously estimated to improve the performance of conventional separate channel estimation. Specifically, an end-to-end strategy over 3-D convolutional neural networks (CNNs) is proposed to estimate multichannel errors collaboratively by fully exploiting the correlation of both innerchannel and intrachannel signals. Furthermore, a simulation-based training data synthesis strategy is proposed to generate training samples with similar signal characteristics with the scene to be reconstructed, by which the proposed 3-D CNN can be well trained without real multichannel signals. Experiments over both simulated and real measured data demonstrate that the proposed deep learning-based channel calibration method can well estimate multichannel errors simultaneously to improve the performance of HRWS SAR imaging.

Index Terms—Channel calibration, convolutional neural networks (CNNs), deep learning, high-resolution wide-swath (HRWS), multichannel synthetic aperture radar (MC-SAR).

I. INTRODUCTION

SYNTHETIC aperture radar (SAR) can provide high-resolution images under various weather and lighting conditions, finding extensive applications in both civilian and military fields. Due to the demand for wide coverage and high-resolution imaging of the Earth's surface, high-resolution and wide-swath (HRWS) imaging technology has attracted increasing attention. The traditional single-channel SAR systems employ a low PRF to transmit signals in order to avoid severe range ambiguity when

achieving wide-swath imaging. However, the low PRF can lead to Doppler ambiguity, thereby reducing the azimuth resolution. To address this conflict between HRWS, the multichannel in azimuth SAR system has been developed, incorporating digital beam forming (DBF) technology. Multichannel in azimuth SAR system works at a lower PRF and utilize multiple receive channels arranged in azimuth to simultaneously receive echo signals. This effectively increases the azimuth sampling rate, allowing for wider swath coverage without compromising resolution. Currently, the satellites TerraSAR-X and TanDEM-X, developed through collaboration between the German Aerospace Center (DLR) and Airbus Defence and Space, operate SAR systems in multichannel mode [1], [2], [3], [4], [5], [6], [7], [8], [9], [10], [11], [12], [13], [14], [15], [16].

During the operation of the system, unavoidable channel errors arise due to nonideal temperature variations and differences in characteristics across each channel. Specifically, channel errors can be categorized into amplitude and phase errors, range sampling time error, antenna position measurement error, and others. Amplitude error refers to the difference in the strength of the received signal among channels, which may be caused by uneven channel gains or nonuniform antenna radiation patterns. Phase error denotes deviation in the phase of the received signal between channels, typically caused by differences in signal transmission paths, differences in electronic component characteristics, etc. Range sampling time error exists due to slight timing differences when signals reach the receiver, resulting from inaccurate clock synchronization or varying lengths of signal transmission paths. Antenna position measurement error reflects physical deviations in channel positions, affecting signal reception direction and beamforming effectiveness. Channel errors degrade the consistency between different channels, and such mismatch severely impacts the signal reconstruction performance and imaging quality of HRWS SAR systems. Therefore, estimating and compensating for channel errors are crucial for multichannel SAR imaging. Currently, there are many methods for estimating channel errors, which can mainly be divided into two categories: time-domain channel phase error correction algorithms and Doppler-domain channel phase error correction algorithms. In Wahl et al.'s [17] work, phase gradient autofocus technique has been carefully studied to estimate the phase error. In Yang et al.'s [18] work, the method in the Doppler domain is proposed to estimate channel errors for multichannel SAR

systems in azimuth without matrix decomposition and inversion processing. However, when the Doppler ambiguity number approaches the number of channels, the noise subspace may disappear, significantly reducing the performance of the phase error estimation algorithm. In Jing et al.'s [19] work, a method for mitigating azimuth ambiguities in the presence of channel errors is proposed, contingent upon an unobstructed Doppler spectrum. Farquharson et al. [20] proposed a contrast-based phase calibration algorithm for DBF remote sensing radars, aimed at correcting time-varying phase errors in antenna arrays. Nevertheless, this algorithm cannot be directly applied to multichannel calibration in HRWS SAR imaging, particularly considering the impact of ambiguity numbers. In Xiang et al.'s [21] work, an image-domain subspace-based channel mismatch calibration and postimaging ambiguity suppression algorithm for MACs SAR is proposed. The baseline error and channel phase error are joint-estimated by the proposed method, achieving a more accurate estimate by iteration. In Huang et al.'s [22] work, a new channel error calibration algorithm for multichannel HRWS-SAR imaging in the Doppler domain has been proposed. It does not need to decompose the covariance matrix of the training samples when estimating the channel phase errors.

Deep learning, as a crucial branch of artificial intelligence, has made significant advancements in recent years. By constructing deep neural network architectures and training them with large datasets, deep learning can automatically learn and extract complex features from data. This has led to breakthroughs in fields, such as image recognition, speech recognition, and natural language processing. Deep learning applications in the radar field are also rapidly advancing. By utilizing deep neural networks to process radar data, more precise target detection, tracking, and classification can be achieved. Deep learning techniques effectively extract features from complex radar data, identifying target shapes, motion patterns, and attributes, thereby enhancing radar system performance and reliability. These advancements are crucial not only for civilian and military applications but also drive the trend toward intelligent and autonomous radar technology. Deep learning performs exceptionally well in regression tasks. The regularization iteration process is described as a convolutional neural network (CNN) used to solve inverse problems. In Wei and Chen's [23] work, a CNN-based technique is proposed to solve full-wave inverse scattering problems, which is aimed at retrieving permittivities of dielectric scatterers from the knowledge of measured scattering data.

In this article, a novel channel-calibration method based on 3-D CNN for multichannel in azimuth SAR system is proposed. 3-D CNN can directly handle multidimensional data, making them particularly suitable for analyzing SAR data that includes channel dimensions. In contrast, traditional time-domain or frequency-domain methods typically focus on a single dimension and may require additional steps to integrate information across different dimensions. The deep structure of 3-D CNN enables automatic learning of complex features within the data without the need for predefined or manually selected features. This differs from traditional methods, which often rely on expert knowledge to choose appropriate signal processing techniques. First, a large simulation dataset is made for network training,

which solves the problem of insufficient SAR data. Then, an end-to-end method based on 3-D CNN for multichannel SAR data is designed to estimate the channel phase errors. The network can take into account the correlation between signals of a single channel and the correlation of data between channels at the same time. The proposed method takes 3-D multichannel cubes as input data, and the phase errors of all channels are directly obtained. Finally, the experiments validate the effectiveness of the proposed channel error estimation method. The estimation accuracy of the method is better than conventional channel phase error estimation methods [9], [15], [21], [22], [23], [24], [25], [26], [27], [28], [29], [30].

In summary, the main contributions of this article are listed as follows.

1) A 3-D CNN-based multichannel error estimation algorithm is proposed for HRWS SAR imaging. As a result, the performance of HRWS SAR imaging can be improved by simultaneously estimate multichannel errors for channel mismatch compensation.
2) The correlation of both innerchannel and intrachannel signals is fully exploited by 3-D convolution for channel error estimation, by which the constructed 3-D CNN can take into account the correlation between signals of a single channel and the correlation of data between channels at the same time.
3) In order to solve the problem of insufficient SAR data for network training, a simulation-based training data synthesis strategy is proposed to generate training samples with similar signal characteristics with the scene to be reconstructed, by which the proposed 3-D CNN can be well trained without real multichannel signals.

The rest of this article is organized as follows. In Section II, the imaging geometry model and the signal error model of the multichannel SAR system are introduced. In Section III, channel calibration framework based on the 3-D CNN is proposed. In Section IV, the experiments of multiple scattering points and real measured data for MC-SAR system are conducted, respectively, to verify the effectiveness of the proposed channel error estimation method. Finally,Section V concludes this article.

II. Geometry Model and Channel Errors for the Multichannel in Azimuth HRWS SAR System

In this section, the imaging geometry model of the multichannel SAR system is first described. Following that, the signal model under ideal conditions and the errors model are introduced, providing a theoretical basis for the subsequent generation of data.

A. Geometry Model

The 3-D geometric model of a multichannel in azimuth HRWS SAR system is shown in Fig. 1(a), where the X-axis represents the moving direction of the radar platform, the Z-axis is away from the center of the Earth, and the Y-axis is perpendicular to the plane formed by the X-axis and the Z-axis. The platform moves along the X-axis at a speed of v, h denotes the height of the platform, and W_r denotes the swath width.
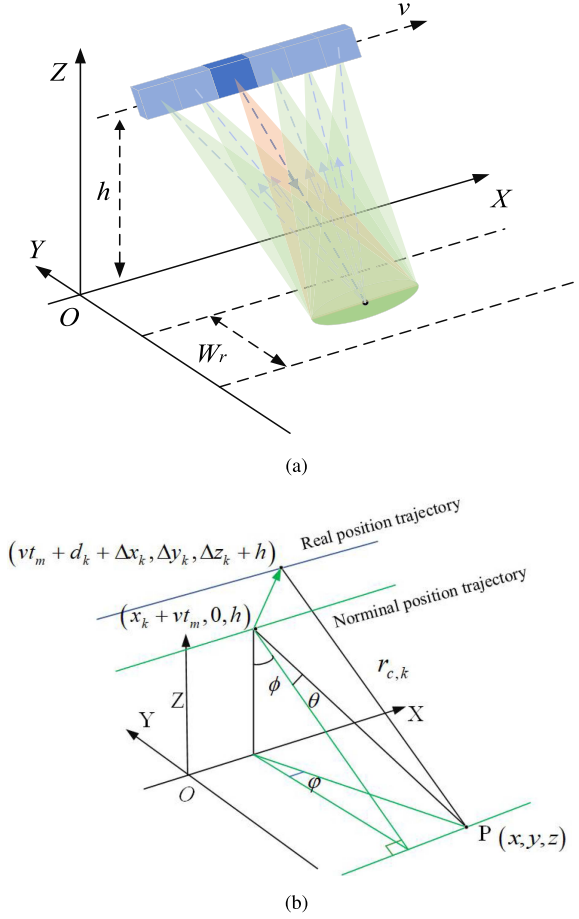
(a)

(b)

Fig. 1. (a) Multichannel in azimuth HRWS SAR system. (b) Geometry model of the kth channel of the multichannel in azimuth HRWS SAR system.

Compared with the traditional single-channel SAR system, the multichannel system employs a strategy utilizing multiple channels in azimuth to simultaneously meet the requirements of wide swath and high azimuth resolution. As shown in Fig. 1(a), the multichannel system consists of six channels moving along the X-axis, where the third channel is responsible for transmitting wide-beam chirp signals, while all the channels receive the echo simultaneously. The transmitting channel is considered as the reference channel. The channels are uniformly distributed, and the distance between adjacent channels is d. The theory of effective phase center (EPC) defines the position in the middle of each channel as the EPC. Therefore, the distance between each EPC can be represented by $d/2$. In practice, the echoes received by each channel can be considered as being transmitted and generated at each EPC by compensating a constant phase relative to the reference channel [31].

The geometry of the kth channel for the multichannel in azimuth HRWS SAR system is shown in Fig. 1(b), in which R_k represents the distance between the kth channel and the target P, also known as the instantaneous slant range, ϕ denotes the depression angle, φ denotes the azimuth angle, and θ denotes the cone angle. The green straight line represents the ideal position trajectory, called nominal trajectory, while the blue line represents the actual position trajectory. In the ideal situation,

the kth channel moves at a constant speed v along the nominal trajectory. Assuming that the coordinates of the reference channel are $(0, 0, h)$ when $t_m = 0$, where t_m represents the slow time in the azimuth direction. Then at time t_m, the coordinates of the kth channel will be $(vt_m + d_k, 0, h)$, where d_k is the baseline length along azimuth between the kth channel and the reference channel. Normally, the reference channel transmits a wideband linear frequency modulation signal. Assuming that the coordinates of the target P are (x, y, z), after EPC processing and range compression, the signal received by the kth channel in the range-frequency and azimuth-time domain can be expressed as

$$s_{c,k}(f_r, t_m) = \iint \sigma(x, y) H(f_r) g\left(t_m - \frac{x - d_k}{v}\right)$$
$$\cdot \exp\left(\frac{-j4\pi(f_c + f_r)R_k(x, y, t_m)}{c}\right) dx dy \tag{1}$$

where

$$R_k(x, y, t_m) = \sqrt{(x - d_k - vt_m)^2 + R_b^2} \tag{2}$$

and $R_b = \sqrt{h^2 + y^2}$ represents the shortest distance from the target P to the motion trajectory of the platform. In (1), $\sigma(x, y)$ denotes the complex reflection coefficient of the scatter (x, y), $H(f_r)$ indicates the window function corresponding to the range frequency after range compression, and $g(t)$ indicates the slow time window function, which reflects the antenna pattern and other azimuth signal characteristics. In addition, f_c, f_r, and c represent carrier frequency of the transmitted signal, range frequency, and the speed of light, respectively.

B. Errors Model

In fact, due to temperature influence, structural differences in antennas with each channel, deviations in channel positions, and sampling time biases, channel errors inevitably occur in multichannel HRWS SAR system. These errors disrupt consistency among channels, greatly reducing imaging performance of the multichannel system. Generally speaking, channel errors typically include amplitude and phase errors, range sampling time error, and antenna position measurement error, etc. Amplitude and phase errors are usually treated as constants. Range sampling time error is a fast time error that appears as a phase error in the range frequency domain. Such error is linear with the range frequency. For the antenna error, Fig. 1(b) illustrates the deviation between the ideal and actual positions. Specifically, if the ideal position of the kth channel at time t_m is $(vt_m + d_k, 0, h)$, the actual position is assumed to be $(vt_m + d_k + \Delta x_k, \Delta y_k, \Delta z_k + h)$, where Δx_k, Δy_k, and Δz_k represent the antenna position measurement errors along the X-axis, Y-axis, and Z-axis of the kth channel, respectively. In practical operations, following range compression and considering the presence of errors, the echo received by the kth channel for the multichannel in azimuth HRWS SAR system in the range-frequency and azimuth-time domain can be expressed

as

$$s'_{c,k}(f_r, t_m) = \iint A_{c,k} \exp(j\Delta\phi_{0,k})\sigma(x,y)H(f_r)$$
$$\cdot g\left(t_m - \frac{x - d_k - \Delta x_k}{v}\right)$$
$$\cdot \exp(-j2\pi f_r \Delta\tau_k)$$
$$\cdot \exp\left(\frac{-j4\pi(f_c + f_r)R'_k(x,y,t_m)}{c}\right)dxdy \tag{3}$$

where

$$R'_k(x,y,t_m) = \Big[(x - d_k - vt_m - \Delta x_k)^2$$
$$+ (y - \Delta y_k)^2 + (h + \Delta z_k)^2\Big]^{\frac{1}{2}}. \tag{4}$$

In (3), $A_{c,k}$ and $\Delta\phi_{0,k}$ denote the amplitude and phase error of the kth channel, respectively. $\Delta\tau_k$ is the range sampling time error, which introduces the linear phase $-2\pi f_r \Delta\tau_k$ in the range-frequency domain. For a multichannel in azimuth SAR system, the variations in antenna position measurement errors tend to be relatively gradual, allowing for the assumption that they remain constant within the synthetic aperture time. Consequently, the values of Δx_k, Δy_k, and Δz_k in the system can be regarded as constants. As can be seen from (4), the antenna position measurement errors can be classified into the azimuth baseline measurement error and the slant-range error. During the installation and position measurement of the antenna, the values of Δx_k, Δy_k, and Δz_k can be meticulously adjusted to remain within the magnitude of 0.01 m, thereby ensuring that the slant range error is also within the same order of magnitude. Considering the range resolution of HRWS SAR images typically spans an order of 1 m, the influence of the slant-range error on the range cell migration can be disregarded. Consequently, the antenna position measurement errors manifest as phase errors in the echoes of multichannel SAR system, as demonstrated by

$$s'_{c,k}(f_r, t_m) = \iint A_{c,k} \exp(j\Delta\phi_{0,k})\sigma(x,y)H(f_r)$$
$$\cdot g\left(t_m - \frac{x - d_k - \Delta x_k}{v}\right)$$
$$\cdot \exp\left\{j\left(\Delta\phi_{1,k} + \Delta\phi_{2,k}(x,y)\right)\right\}$$
$$\cdot \exp(-j2\pi f_r \Delta\tau_k)$$
$$\cdot \exp\left(\frac{-j4\pi(f_c + f_r)R''_k(x,y,t_m)}{c}\right)dxdy \tag{5}$$

where

$$R''_k(x,y,t_m) = \sqrt{(x - d_k - vt_m - \Delta x_k)^2 + y^2 + h^2}. \tag{6}$$

In (5), the term $\Delta\phi_{1,k} + \Delta\phi_{2,k}(x,y)$ represents the phase error induced by the antenna position measurement errors in the kth channel. This comprises a constant phase error component $\Delta\phi_{1,k}$ and a variable phase error component $\Delta\phi_{2,k}(x,y)$, which varies with range. The azimuth baseline measurement error, denoted as Δx_k in (5) and (6), can be precisely estimated through the baseline measurement error estimation algorithm. By applying the Doppler ambiguity suppression algorithm to reconstruct an unambiguous Doppler spectrum, the effects of Δx_k can be substantially neutralized. When estimating the range-invariant phase error $\Delta\phi_{2,k}(x,y)$, the echoes can be segmented into blocks along the range direction. In this way, the range-invariant phase error can be approximately regarded as a constant within each range block. Consequently, this article does not focus on it as the primary research target. Instead, this study investigates the estimation of constant errors across different channels.

III. 3-D CNN-BASED CHANNEL ERROR ESTIMATION ALGORITHM FOR MULTICHANNEL IN AZIMUTH HRWS SAR SYSTEM

Fig. 2 illustrates the proposed channel calibration framework based on a 3-D CNN for multichannel in azimuth HRWS SAR system. The original data consists of echoes in the range-frequency and azimuth-time domain from a multichannel in azimuth HRWS SAR system under ideal position trajectory, with the signal form of the kth channel, as shown in (1). This original data is utilized to generate actual multichannel SAR echoes with channel errors, which are then used for the training and testing of the 3-D CNN. The training groups generated serve as the input for the 3-D CNN, with their corresponding labels forming the output of the 3-D CNN. Initially, the network computes the output through forward propagation, and then calculates the error between predicted and true values using the loss function. Subsequently, the back-propagation algorithm is applied to propagate the error from the output layer back to the input layer, updating the weights and biases of each layer. This process involves multiple iterations and optimization algorithms to minimize the loss function, thereby enhancing the model's predictive accuracy. Leveraging the training dataset, the proposed 3-D CNN undergoes training through the minimization of the loss function, enabling the calculation of optimal parameters. Consequently, the proposed 3-D CNN learns to map the training groups to their corresponding labels, which represent the channel errors. As a result, the trained 3-D CNN serves as the error estimation processor. Once the training phase is completed, the network's parameters are set, allowing the 3-D CNN to predict channel errors in testing dataset where these errors are unknown. Subsequently, these channel errors will be corrected. Following the reconstruction of the multichannel signal, the SAR image can be obtained using conventional imaging algorithms.

A. Training Data Generation

Due to the scarcity of actual multichannel HRWS SAR data, we have generated a large volume of data based on geometry and signal models. These data are divided into two categories: one for network training and the other for testing. This approach helps to compensate for the lack of data, enhancing the training effectiveness of the model and the reliability of the tests. Pairs
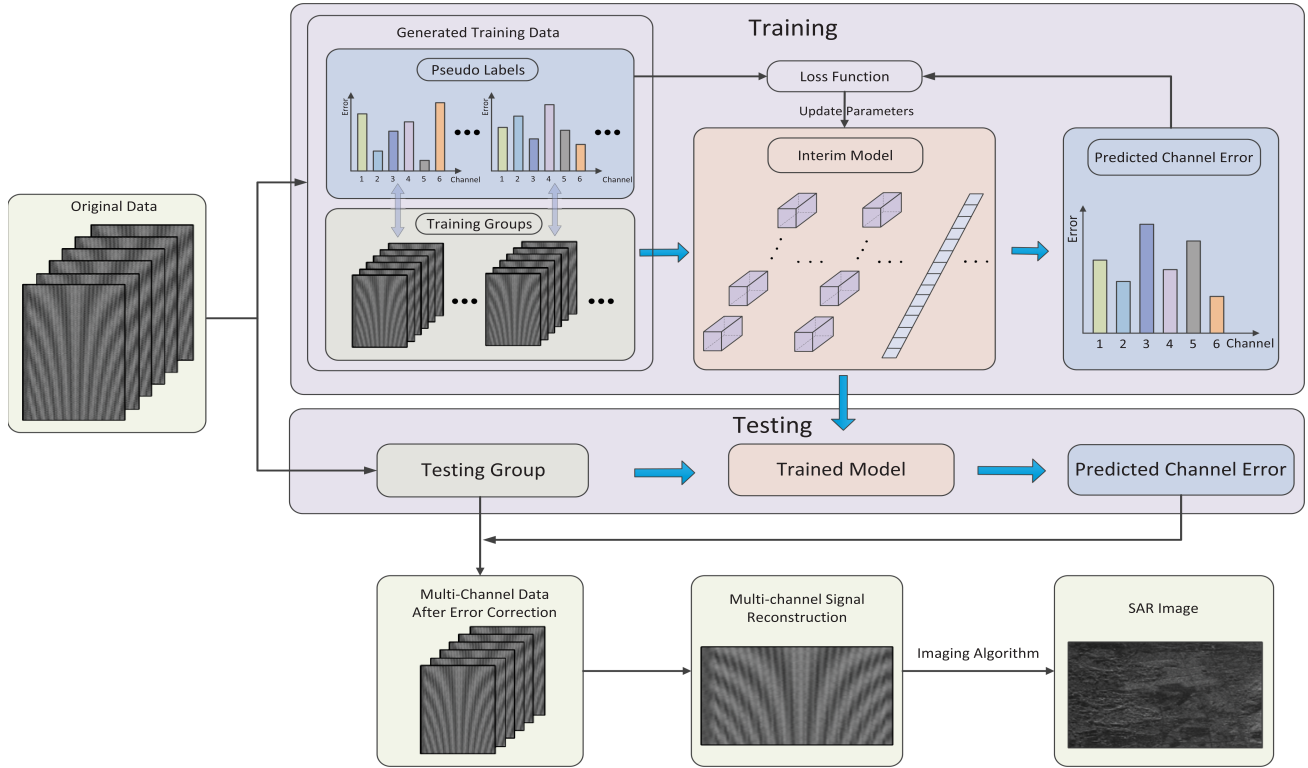
Fig. 2. Channel-calibration framework based on 3-D CNN.

of training groups and their corresponding labels are essential for the training of the network.

The dataset $\boldsymbol{X} = \{\boldsymbol{x_1}, \boldsymbol{x_2}, \ldots, \boldsymbol{x_N}\} \in \mathbb{C}^{M \times N_1 \times C}$ contains N labeled cube data, where the element $\boldsymbol{x}$ is a 3-D complex matrix representing the echoes received by the multichannel SAR system, M represents the number of sampling points in the range direction of the multichannel SAR system, N_1 represents the number of azimuth sampling points, and C is the number of channels of the system. $\boldsymbol{Y} = \{\boldsymbol{y_1}, \boldsymbol{y_2}, \ldots, \boldsymbol{y_N}\} \in \mathbb{R}^{1 \times 1 \times C}$ is the set of corresponding label vectors, representing the channel errors of each channel relative to the reference channel. Therefore, the number of elements in $\boldsymbol{y}$ matches the number of channels.

In a pair of training data, the input of the network $\boldsymbol{x}$ is the original data with channel errors. It can be simulated using the geometry model and channel errors model of the multichannel SAR system. The signal form of a dimension corresponding to the channels is as shown in (5). Such multichannel 3-D data can be input into the network in the form of cubes. The output corresponding to the network input is a vector $\boldsymbol{y}$, whose number of elements is the number of channels, and the value of each element is the phase error of the corresponding channel. The input data $\boldsymbol{x}$ of the 3-D CNN can be generated by

$$\boldsymbol{x} = s_c \cdot e^{j\boldsymbol{y}} \tag{7}$$

where s_c is the echo in the range-frequency and azimuth-time domain from a multichannel in azimuth HRWS SAR system under ideal position trajectory, where the data of a dimension corresponding to the channels $s_{c,k}$ is as shown in (1). The values

of the elements in $\boldsymbol{y}$ are randomly and uniformly distributed over a certain range. In the experiments conducted in this article, the values of channel errors range within $[-90°, 90°]$. A total of 500 data pairs were generated, of which 400 pairs were used for training and 100 pairs for testing.

B. 3-D CNN Architecture

The structure of the proposed 3-D CNN is illustrated in Fig. 3, with conv and f_c representing the 3-D convolution and fully connected layer, respectively. Fig. 4 depicts the layer block, featuring 3-D batch normalization and rectified linear unit. The input data samples in 3-D have dimensions of $2048 \times 256 \times 6$. In the first convolutional layer, layer1, 18 kernels of size $3 \times 3 \times 3$ with a stride of $(2, 2, 1)$ convolves the input volume, resulting in 18 feature cubes of size $1023 \times 127 \times 6$. This process simultaneously considers the correlation between signals within a single channel and the correlation of data between channels due to the 18 kernels used. Following the convolutional layer, the feature cubes are reduced to dimensions of 18 $1 \times 1 \times 6$ through pooling operations. Subsequently, a flattening operation converts these feature volumes into a $1 \times 1 \times 108$ feature vector. Finally, the network employs three fully connected layers to generate an output vector.

To maintain the appropriate size of the feature cubes during operations, padding is utilized in the 3-D CNN. Moreover, the mean squared error (MSE) loss function is employed for training
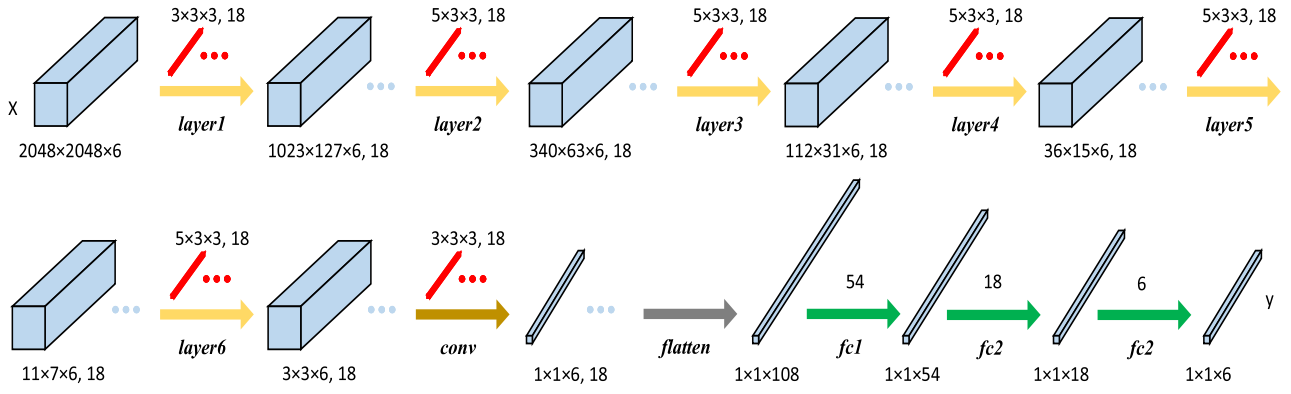
Fig. 3. Network structure of 3-D CNN.

TABLE I
SIMULATION PARAMETERS FOR SINGLE SCATTERING POINT EXPERIMENTS

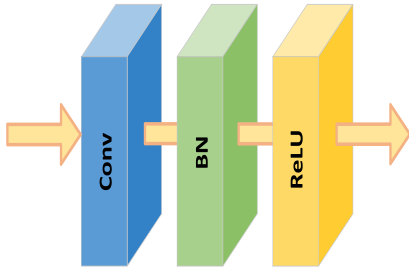|			
Carrier frequency	9.7 GHz	Channel number	6
Platform velocity	500 m/s	Bandwidth of transmitted signal	160 MHz
Range sampling rate	200 MHz	Nearest slant range	7000 m
Pulse width	10 us	Azimuth length of antenna	0.375 m

Fig. 4. Architecture of the layer block.

the network. The MSE loss function is defined as

$$L(\boldsymbol{y}, \boldsymbol{y}') = \frac{1}{n} \sum_{i=1}^{n} (\boldsymbol{y}_i - \boldsymbol{y}'_i)^2 \qquad (8)$$

where $\boldsymbol{y}_i$ denotes the estimated value and $\boldsymbol{y}'_i$ denotes the real channel error.

IV. EXPERIMENTAL RESULTS AND ANALYSIS

In this section, experiments of multiple scattering points and real measured data for MC-SAR system are conducted respectively to verify the effectiveness of the proposed channel error estimation method.

A. Experiments of Simulated Multichannel in Azimuth HRWS SAR Data With Channel Errors

In the experiment, the training data are obtained by an airborne experiment with a six-channel in azimuth SAR system. The system parameters are shown in Table I.

In the simulation experiment, the data are obtained by an airborne experiment with a six-channel in azimuth SAR system. The system parameters are shown as follows: the velocity v of the platform is 500 m/s, the distanced between the two neighboring channels is 0.375 m, the distance R_b between the platform and the scatter located in the middle of the scene is 7000 m. The distribution of the antennas is along track, the middle antenna transmits chirp signals and all of antennas receive echoes. The Doppler bandwidth is approximately 2664.3 Hz. The simulated data is with channel mismatch in phase. In order to illustrate the effectiveness of the the proposed error correction algorithm, multiple scattering points experiments are designed. The scattering points distribution of the scene is shown in Fig. 5(a), which is the result of imaging by range-Doppler (RD) algorithm using the data simulated by six-channel SAR system, where the stationary clutter points are not shown. Then, randomly generated channel errors are added to the original data, and the imaging results are as shown in Fig. 5(b). Because the channels are evidently mismatched, there are obvious ambiguous components in the SAR image, which degrade imaging performance.

In the experiment, three channel error estimation algorithms, which are subspace-based channel error correction method, correlation function channel method, and the proposed method in this article, are utilized to estimate the channel errors in phase. The estimated deviation for the channel mismatch in phase is defined as

$$\text{De} = |\varphi - \hat{\varphi}| \qquad (9)$$

where φ denotes the real channel mismatch in phase, and $\hat{\varphi}$ is the estimated channel mismatch in phase.

The results of channel error estimation using subspace-based method, correlation function method, and the proposed method
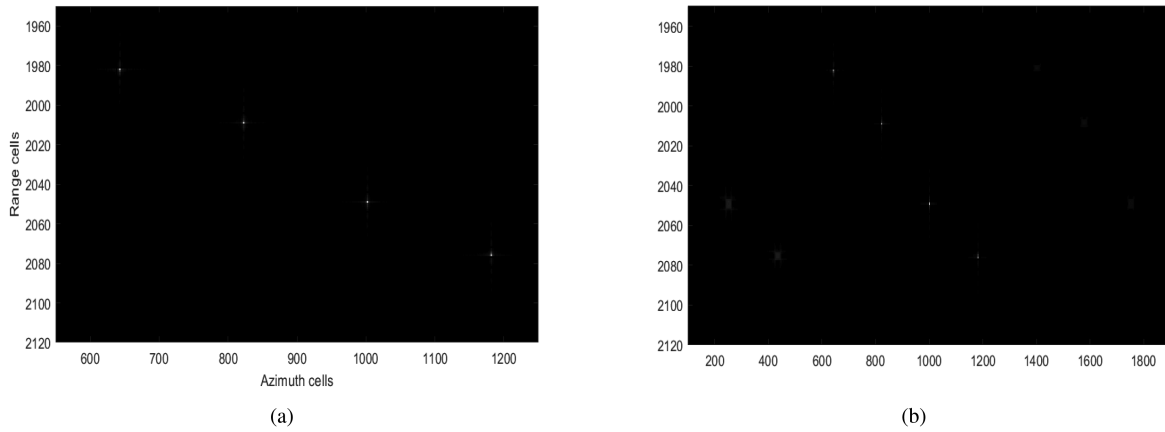
Fig. 5. Experimental results of SAR imaging. (a) Distribution of scattering points in the scene. (b) Six-channel moving target imaging result using RD with channel errors.

TABLE II
ERROR ESTIMATION RESULTS BY SUBSPACE-BASED METHOD

Channel number	Group 1		Group 2	
	Real value	Estimated value	Real value	Estimated value
Channel 1	−36.18	−38.20	64.72	60.62
Channel 2	−43.90	−40.88	85.02	85.19
Channel 3	0	0.30	0	0.30
Channel 4	−9.57	−9.32	71.98	70.90
Channel 5	56.87	56.20	4.33	4.81
Channel 6	−72.29	−68.25	−68.36	−68.29

TABLE III
ERROR ESTIMATION RESULTS BY CORRELATION FUNCTION METHOD

Channel number	Group 1		Group 2	
	Real value	Estimated value	Real value	Estimated value
Channel 1	−39.87	−38.80	82.29	82.09
Channel 2	82.35	81.95	−2.63	−2.33
Channel 3	0	0.20	0	0.20
Channel 4	83.67	83.60	54.05	53.85
Channel 5	−61.62	−61.42	−64.46	−64.26
Channel 6	84.70	84.40	−14.08	−14.38

TABLE IV
ERROR ESTIMATION RESULTS BY THE PROPOSED METHOD

Channel number	Group 1		Group 2	
	Real value	Estimated value	Real value	Estimated value
Channel 1	23.12	23.16	70.45	70.41
Channel 2	−30.23	−30.18	22.35	22.38
Channel 3	0	0.01	0	0.01
Channel 4	50.76	50.75	−30.36	−30.35
Channel 5	40.20	40.24	2.52	2.50
Channel 6	−5.65	−5.70	−40.89	−40.93

are presented in Tables II–IV, respectively. As can be seen from above-mentioned tables, for each algorithm, two sets of random errors are generated for error estimation. In Table II, it can be seen that there is a small deviation between the real value and the estimated value using subspace-based method. Typically, the deviation is less than 5 °. In Table III, the capability of error estimation capability is further improved. It can be seen that the level of the estimated deviation is less than 2 °. In Table IV, the level of the estimated deviation for the proposed approach is less than 0.08 °. Based on the data presented in the tables, it can be
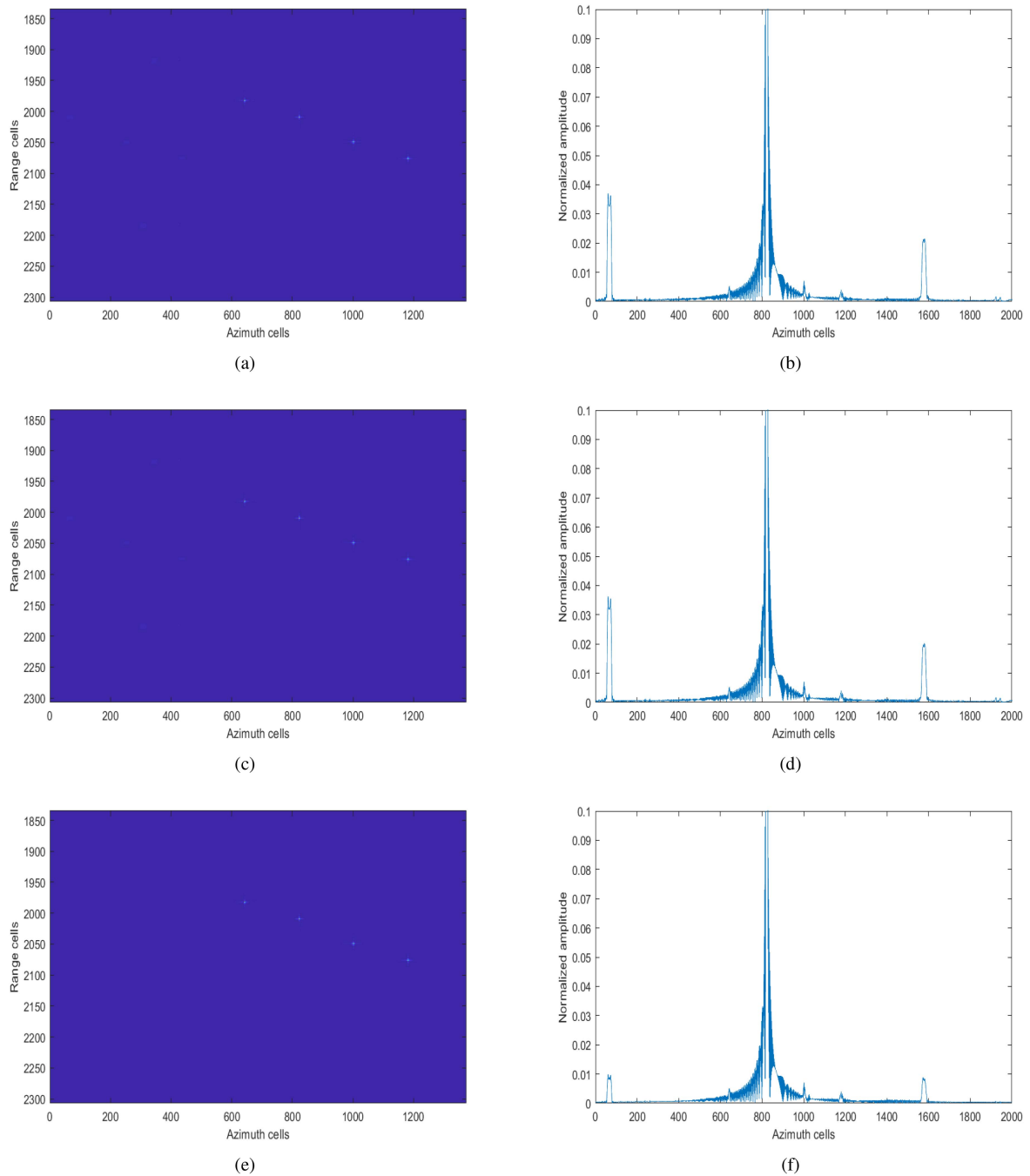
Fig. 6. Experimental results of SAR imaging after channel correction. (a) Imaging result by RD algorithm after channel correction using subspace-based method. (b) Cross-sectional view of a certain range cell from (a). (c) Imaging result by RD algorithm after channel correction using correlation function method. (d) Cross-sectional view of a certain range cell from (c). (e) Imaging result by RD algorithm after channel correction using the proposed method. (f) Cross-sectional view of a certain range cell from (e).

observed that among the three methods, the proposed method exhibits the best accuracy in error estimation.

In order to display the results of channel error correction more intuitively, Fig. 6 shows the imaging results by RD algorithm after channel correction using the three methods. As can be seen from Fig. 6(a), after error correction by subspace-based method, the ambiguous components of the targets have been basically eliminated. However, there are still slight bright spots in the image, which are the results of channel error influence, indicating

that there are residual channel errors. Fig. 6(b) further shows a cross-sectional view of a certain range cell from Fig. 6(a). For ease of observation, the amplitude values are presented within the range of [0, 0.1]. It is evident that, in addition to the primary peak representing the target, there are also weaker peaks, which are the image blurring caused by channel errors, indicating that the errors have not been entirely corrected. Fig. 6(c) is the imaging result by RD algorithm after channel correction using the correlation function method. Similarly to Fig. 6(a), Fig. 6(c) also
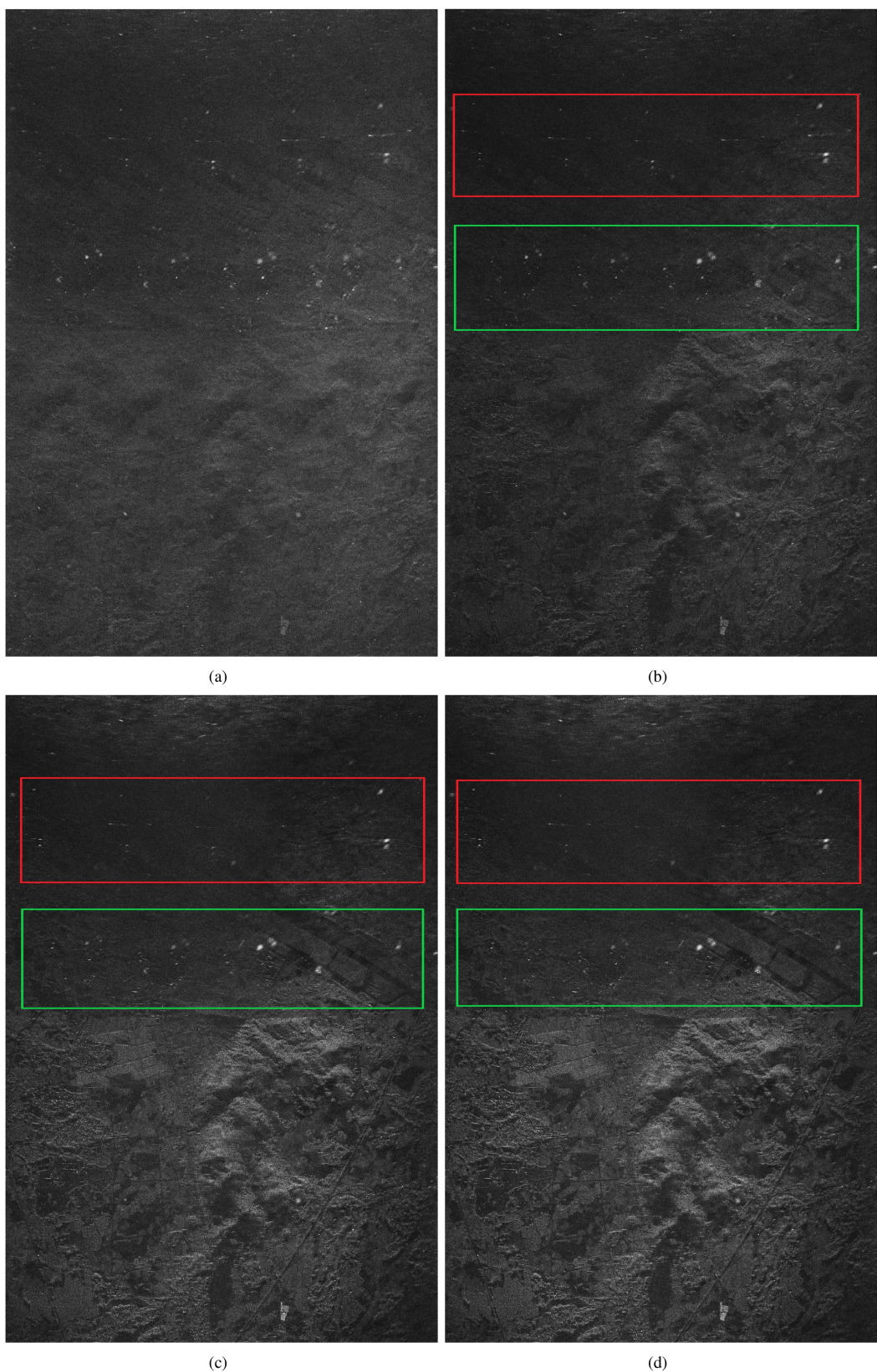
Fig. 7. Experimental results of real measured data after the channel calibration using different algorithms. (a) Imaging result without channel calibration. (b) Imaging result using subspace-based method. (c) Imaging result using correlation function method. (d) Imaging result using the proposed method.

shows slight bright blocks, indicating the presence of residual channel errors. When extracting amplitude information from a certain range cell, as shown in Fig. 6(d), minor peaks can be observed in addition to the primary peak. Slightly differing from Fig. 6(b), the energy of the minor peaks in Fig. 6(d) is slightly reduced. Fig. 6(e) is the imaging result after channel correction using the proposed method. Compared with Fig. 6(a) and (c), there are no visible bright spots other than the targets in Fig. 6(e), indicating minimal ambiguous components. Furthermore, a certain range cell at the same location is extracted and amplitude information is displayed in Fig. 6(f). It can be clearly seen that compared with Fig. 6(b) and (d), the amplitude values of the slight peaks in Fig. 6(f) have been greatly reduced and are almost nonexistent, indicating that the channel errors are nearly eliminated. From the above-mentioned simulation experiment analysis, it can be concluded that the proposed algorithm has the best error estimation performance.

B. Experiments of Real Measured Data for the Proposed Channel-Calibration Algorithm

In order to explicitly prove the effectiveness of the proposed algorithm, experiments of real measured data are designed. The real measured data are obtained by an airborne experiment with a multichannel in azimuth HRWS SAR system. The system works in the side-looking and Scan-SAR mode. The distribution of the antennas is along azimuth, the middle antenna transmits chirp signals and all of the antennas receive echoes.

After the channel calibration using different algorithms, imaging results are presented in Fig. 7. Fig. 7(a) represents the imaging result without channel errors correction. As can be observed, the presence of channel errors has resulted in a serious mismatch between channels, which has led to the image appearing with obvious ambiguous components, making it impossible to clearly see the geomorphic features reflected in the image. Fig. 7(b) shows the imaging result after the channel calibration using the subspace-based method. Compared with Fig. 7(a), it can be observed that the ambiguous components have been significantly reduced, and the basic landform conditions can be clearly seen. However, the ambiguous components of the strong scattering points remain evident, indicating that residual channel errors are considerable and have a significant impact on the imaging quality. Fig. 7(c) is the imaging result after the channel calibration using the correlation function method. Compared with Fig. 7(b), the ambiguous components in Fig. 7(c) is slightly decreased, but still exists. This indicates that while correlation function method provides a higher precision in error estimation compared to subspace-based method, the estimated error values are not very accurate, resulting in residual channel errors after the channel calibration. The imaging result after the channel calibration using the proposed method is shown in Fig. 7(d). Compared with Fig. 7(a)–(d) is much clearer, with most of the ambiguous components suppressed. This indicates that after error correction, most of the channel errors are corrected, and the residual errors using the proposed method are the smallest.

In order to further compare the imaging effects after channel error correction using each algorithm, the strong scatters area
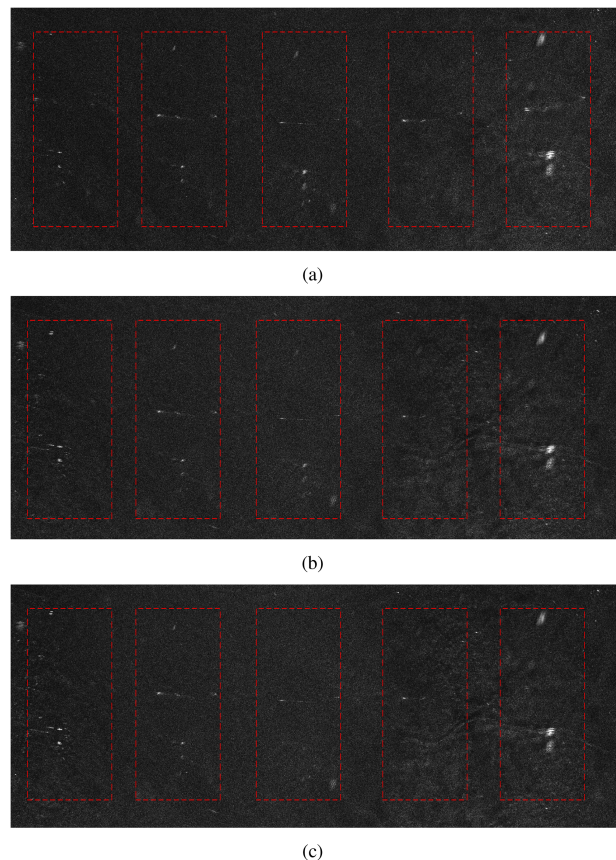

(a)

(b)

(c)

Fig. 8. Local enlargement images for area surrounded by red boxes in Fig. 7. (a) Imaging result using subspace-based method. (b) Imaging result using correlation function method. (c) Imaging result using the proposed method.

surrounded by red boxes in Fig. 7(b)–(d) is displayed in Fig. 8. Fig. 8(a)–(c) is local enlargement images for area surrounded by red boxes in Fig. 7(b)–(d), respectively. The strong scatters and their ambiguous components are marked within the red dashed boxes. From Fig. 8(a), we can see the obvious ambiguous components of strong scatters, which indicates that the larger residual channel errors has not been corrected. Compared with Fig. 8(a), the energy of the ambiguous component in Fig. 8(b) is significantly reduced, the outline of the landform is much clearer, and the scatters components in the first red box and the fourth red box are greatly reduced. This indicates that the residual channel errors in Fig. 8(b) is smaller than in Fig. 8(a). Compared with Fig. 8(b) and (c) exhibits a clearer geomorphic outline. The ambiguous components within the third red box, both at the top and bottom, have disappeared directly, indicating that the channel errors correction in Fig. 8(c) is more thorough.

Consequently, the strong scatters area surrounded by green boxes in Fig. 7(b)–(d) is displayed in Fig. 9. Fig. 9(a)–(c) is local enlargement images for area surrounded by green boxes in Fig. 7(b)–(d), respectively. The strong scatters and their ambiguous components are marked within the green dashed boxes. It can be observed that Fig. 9(a) exhibits strong ambiguous components, making it impossible to clearly see the terrain contours. This indicates the presence of significant residual channel errors. Compared with Fig. 9(a), the energy of the ambiguous
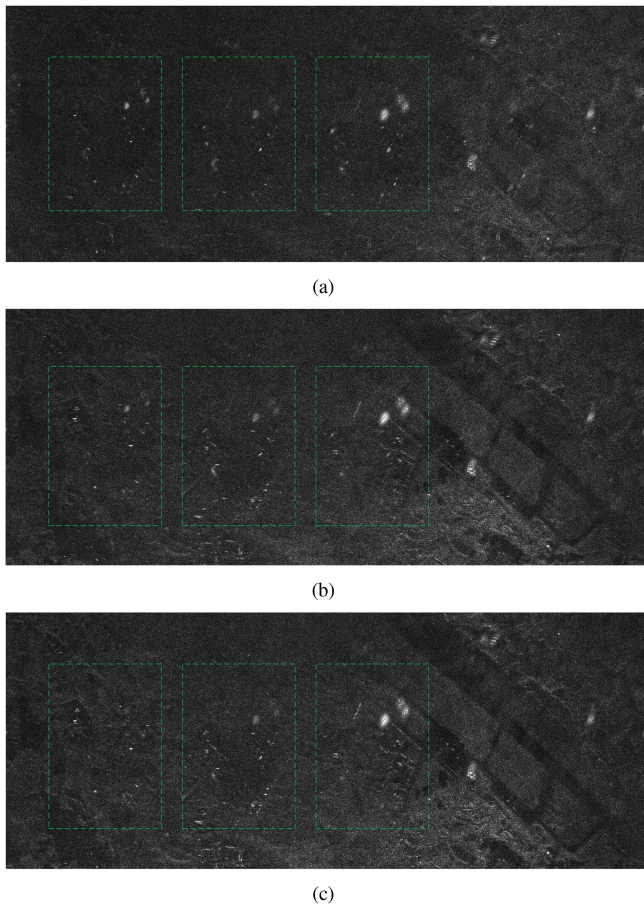
(a)

(b)

(c)

Fig. 9. Local enlargement images for area surrounded by green boxes in Fig. 7. (a) Imaging result using subspace-based method. (b) Imaging result using correlation function method. (c) Imaging result using the proposed method.

component in Fig. 9(b) is significantly reduced, the outline of the landform is much clearer, and the scatters components in the first green box and are greatly reduced. This indicates that the residual channel errors in Fig. 9(b) is smaller than in Fig. 9(a). Compared with Fig. 9(b), all ambiguous components in Fig. 9(c) are greatly reduced, and the terrain outline is clearer. Many ambiguous components within the first and third green boxes have disappeared directly, indicating that the channel errors correction in Fig. 9(c) is more thorough. In summary, among all compared methods, the method proposed in this article has the strongest error estimation ability.

V. Conclusion

The unavoidable channel errors always exist in an HRWS SAR system and may deteriorate the HRWS imaging performance. In this article, we proposed a channel-calibration method based on 3-D CNN for the first time. The network can take into account the correlation between signals of a single channel and the correlation of data between channels at the same time. As a result, the correlation of both innerchannel and intrachannel signals is fully exploited by 3-D convolution for channel error estimation and the performance of HRWS SAR imaging can be improved. The experiments of multiple scattering points and real measured data for MC-SAR system are conducted, respectively, to verify the effectiveness of the proposed method. The accuracy of error estimation of the proposed algorithm is better than that of correlation function method and subspace-based method.

References

[1] H. Yu, S. Yang, S. Zhou, and Y. Sun, "VS-LSDET: A multiscale ship detector for spaceborne SAR images based on visual saliency and lightweight CNN," *IEEE J. Sel. Topics Appl. Earth Observ. Remote Sens.*, vol. 17, pp. 1137–1154, 2024.

[2] P. Huang, H. Yang, Z. Zou, X.-G. Xia, G. Liao, and Y. Zhang, "Range-ambiguous sea clutter suppression for multichannel spaceborne radar applications via alternating APC processing," *IEEE Trans. Aerosp. Electron. Syst.*, vol. 59, no. 5, pp. 6954–6970, Oct. 2023.

[3] J. Li, Z. Xu, Z. Li, Z. Zhang, B. Zhang, and Y. Wu, "An unsupervised CNN-based multichannel interferometric phase denoising method applied to tomoSAR imaging," *IEEE J. Sel. Topics Appl. Earth Observ. Remote Sens.*, vol. 16, pp. 3784–3796, Apr. 2023.

[4] B. Zhang, G. Xu, R. Zhou, H. Zhang, and W. Hong, "Multi-channel back-projection algorithm for mmWave automotive MIMO SAR imaging with Doppler-division multiplexing," *IEEE J. Sel. Topics Signal Process.*, vol. 17, no. 2, pp. 445–457, Mar. 2023.

[5] W. Wang, J. Wang, D. Quan, M. Yang, J. Sun, and B. Lu, "PolSAR image classification via a multi-granularity hybrid CNN-VIT model with external tokens and cross-attention," *IEEE J. Sel. Topics Appl. Earth Observ. Remote Sens.*, vol. 17, pp. 8003–8019, Apr. 2024.

[6] J. Guo, J. Chen, W. Liu, C. Li, and W. Yang, "An improved airborne multichannel SAR imaging method with motion compensation and range-variant channel mismatch correction," *IEEE J. Sel. Topics Appl. Earth Observ. Remote Sens.*, vol. 13, pp. 5414–5423, Sep. 2020.

[7] T. Yang, Z. Li, Y. Liu, Z. Suo, and Z. Bao, "Channel error estimation methods for multi-channel HRWS SAR systems," in *2013 IEEE Int. Geosci. Remote Sens. Symp.*, Melbourne, VIC, Australia, 2013, pp. 4507–4510.

[8] X. Guo, Y. Gao, K. Wang, and X. Liu, "Improved channel error calibration algorithm for azimuth multichannel SAR systems," *IEEE Geosci. Remote Sens. Lett.*, vol. 13, no. 7, pp. 1022–1026, Jul. 2016.

[9] Y. Zhou et al., "A novel approach to Doppler centroid and channel errors estimation in azimuth multi-channel SAR," *IEEE Trans. Geosci. Remote Sens.*, vol. 57, no. 11, pp. 8430–8444, Nov. 2019.

[10] P. Huang, X.-G. Xia, X. Liu, X. Jiang, J. Chen, and Y. Liu, "A novel baseline estimation method for multichannel HRSW SAR system," *IEEE Geosci. Remote Sens. Lett.*, vol. 16, no. 12, pp. 1829–1833, Dec. 2019.

[11] L. Zhang, Y. Gao, and X. Liu, "Robust channel phase error calibration algorithm for multichannel high-resolution and wide-swath SAR imaging," *IEEE Geosci. Remote Sens. Lett.*, vol. 14, no. 5, pp. 649–653, May 2017.

[12] Y. Cai, Y. Deng, H. Zhang, R. Wang, Y. Wu, and S. Cheng, "An image-domain least l1-norm method for channel error effect analysis and calibration of azimuth multi-channel SAR," *IEEE Trans. Geosci. Remote Sens.*, vol. 60, 2022, Art. no. 5222914.

[13] C. Tang, T. Ni, Y. Bai, X. Li, C. Sun, and C. Li, "A novel phase bias calibration algorithm for multi-channel HRWS SAR system in Azimuth," in *2023 4th China Int. SAR Symp.*, 2023, pp. 1–4.

[14] Y. Cai et al., "An efficient phase error calibration method for Azimuth multichannel SAR based on least spectrum difference," *IEEE Trans. Geosci. Remote Sens.*, vol. 62, 2024, Art. no. 5207213.

[15] S.-X. Zhang, M.-D. Xing, X.-G. Xia, Y.-Y. Liu, R. Guo, and Z. Bao, "A robust channel-calibration algorithm for multi-channel in azimuth HRWS SAR imaging based on local maximum-likelihood weighted minimum entropy," *IEEE Trans. Image Process.*, vol. 22, no. 12, pp. 5294–5305, Dec. 2013.

[16] G. Xu, B. Zhang, H. Yu, J. Chen, M. Xing, and W. Hong, "Sparse synthetic aperture radar imaging from compressed sensing and machine learning: Theories, applications, and trends," *IEEE Geosci. Remote Sens. Mag.*, vol. 10, no. 4, pp. 32–69, Dec. 2022.

[17] D. Wahl, P. Eichel, D. Ghiglia, and C. Jakowatz, "Phase gradient autofocus-a robust tool for high resolution SAR phase correction," *IEEE Trans. Aerosp. Electron. Syst.*, vol. 30, no. 3, pp. 827–835, Jul. 1994.

[18] T. Yang, Z. Li, Y. Liu, and Z. Bao, "Channel error estimation methods for multichannel SAR systems in azimuth," *IEEE Geosci. Remote Sens. Lett.*, vol. 10, no. 3, pp. 548–552, May 2013.

[19] W. Jing, M. Xing, Y. Li, and Z. Bao, "Method of removing azimuth ambiguities with channel errors," *Syst. Eng. Electron*, vol. 30, no. 11, pp. 2045–2049, 2008.

[20] G. Farquharson, P. Lopez-Dekker, and S. J. Frasier, "Contrast-based phase calibration for remote sensing systems with digital beamforming antennas," *IEEE Trans. Geosci. Remote Sens.*, vol. 51, no. 3, pp. 1744–1754, Mar. 2013.

[21] J. Xiang et al., "A robust image-domain subspace-based channel error calibration and postimaging reconstruction algorithm for multiple azimuth channels SAR," *IEEE Trans. Geosci. Remote Sens.*, vol. 60, 2022, Art. no. 5215818.

[22] H. Huang et al., "A novel channel errors calibration algorithm for multichannel high-resolution and wide-swath SAR imaging," *IEEE Trans. Geosci. Remote Sens.*, vol. 60, 2022, Art. no. 5201619.

[23] Z. Wei and X. Chen, "Deep-learning schemes for full-wave nonlinear inverse scattering problems," *IEEE Trans. Geosci. Remote Sens.*, vol. 57, no. 4, pp. 1849–1860, Apr. 2019.

[24] L. Zhang, Z. Qiao, M.-d. Xing, L. Yang, and Z. Bao, "A robust motion compensation approach for UAV SAR imagery," *IEEE Trans. Geosci. Remote Sens.*, vol. 50, no. 8, pp. 3202–3218, Aug. 2012.

[25] T. Fang, H. Zhang, D. Liang, L. Zhang, and H. Fan, "A channel phase error estimation method for multichannel tops and multichannel sliding spotlight SAR imaging," *IEEE Geosci. Remote Sens. Lett.*, vol. 19, 2022, Art. no. 4010505.

[26] H. Su, Q. Bao, and Z. Chen, "ADMM–Net: A deep learning approach for parameter estimation of chirp signals under sub-Nyquist sampling," *IEEE Access*, vol. 8, pp. 75714–75727, 2020.

[27] B. Yonel, E. Mason, and B. Yazici, "Deep learning for waveform estimation and imaging in passive radar," *IET Radar, Sonar Navigation*, vol. 13, no. 6, pp. 915–926, 2019.

[28] H. Mu, Y. Zhang, C. Ding, Y. Jiang, M. H. Er, and A. C. Kot, "Deepimaging: A ground moving target imaging based on CNN for SAR-GMTI system," *IEEE Geosci. Remote Sens. Lett.*, vol. 18, no. 1, pp. 117–121, Jan. 2021.

[29] S.-X. Zhang et al., "Multichannel HRWS SAR imaging based on range-variant channel calibration and multi-Doppler-direction restriction ambiguity suppression," *IEEE Trans. Geosci. Remote Sens.*, vol. 52, no. 7, pp. 4306–4327, Jul. 2014.

[30] H. Su, Q. Bao, and Z. Chen, "Parameter estimation processor for chirp signals based on a complex-valued deep neural network," *IEEE Access*, vol. 7, pp. 176278–176290, 2019.

[31] G. Krieger, N. Gebert, and A. Moreira, "Unambiguous SAR signal reconstruction from nonuniform displaced phase center sampling," *IEEE Geosci. Remote Sens. Lett.*, vol. 1, no. 4, pp. 260–264, Oct. 2004.

Yuchen Lin received the B.S. degree in measurement and control technology and instruments from the School of Automation, Northwestern Polytechnical University, Xi'an, China, in 2020. He is currently working toward the M.S. degree in information and communication engineering with Northwestern Polytechnical University, Xi'an.

His research interests include synthetic aperture radar, with application to remote sensing.

Hongtao Zhan was born in Jiangxi, China, in 1999. He received the B.S. degree in communication engineering from Harbin Engineering University, Harbin, China, in 2019, and the M.S. degree in electronics and communication engineering from Xidian University, Xi'an, China, in 2022. He is currently working toward the Ph.D. degree in information and communication engineering with Northwestern Polytechnical University, Xi'an.

His research interests include synthetic aperture radar (SAR) imaging and SAR interference suppression.
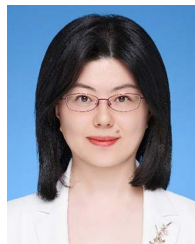
Shuai Wan (Member, IEEE) received the B.E. degree in telecommunication engineering and the M.E. degree in communication and information systems from Xidian University, Xi'an, China, in 2001 and 2004, respectively, and the Ph.D. degree in electronics engineering from the Queen Mary University of London, London, U.K., in 2007.

She is currently a Professor with Northwestern Polytechnical University, Xi'an and an Adjunct Professor with RMIT University, Melbourne VIC, Australia. Her research interests include point cloud compression, versatile video coding, neural networks-based video coding, and multimedia processing.

Shaojie Li was born in Shanxi, China, in 1994. He received the B.S. degree in communication engineering from Xi'an Technological University, Xi'an, China, in 2016. He is currently working toward the Ph.D. degree in information and communication engineering with the School of Electronics and Information, Northwestern Polytechnical University, Xi'an.

His research focuses on SAR imaging.

Shuangxi Zhang (Member, IEEE) was born in Fujian Province, China, 1984. He received the B.S. degree in technique of measuring control and instrument engineering from Xidian University, Xi'an, China, in 2008, and the Ph.D. degree in signal processing from the National Key Lab of Radar Signal Processing, Xidian University, in 2014.

He is currently an Associate Professor with the School of Electronics and information, Northwestern Polytechnical University, Xi'an. From 2014 to 2016, he was a Research Fellow with National University of Singapore, Singapore. His research interests include SAR imaging, SAR interference suppression, array signal processing, and electromagnetic scattering.

Dr. Zhang is the Organizer and Session Chairs of Synthetic Aperture Radar Techniques and Applications-Part1/2 and -Part2/2 in ACES-China 2017, Suzhou, China.

Shaohui Mei (Senior Member, IEEE) received the B.S. degree in electronics and information engineering and the Ph.D. degree in signal and information processing from Northwestern Polytechnical University, Xi'an, China, in 2005 and 2011, respectively.

He is currently a Professor with the School of Electronics and Information, Northwestern Polytechnical University. From 2007 to 2008, he was a Visiting Student with the University of Sydney, Camperdown, NSW, Australia. His research interests include hyperspectral remotesensing image processing and applications, intelligent signal and information acquisition and processing, video processing, and pattern recognition.

Dr. Mei was the recipient of the First prize of Natural Science Award of Shaanxi Province in 2022, the Excellent Doctoral Dissertation Award of Shaanxi Province in 2014, the Best Paper Award of the IEEE International Symposium on Intelligent Signal Processing and Communication Systems (ISPACS) in 2017, the Best Reviewer of the IEEE JOURNAL OF SELECTED TOPICS IN APPLIED EARTH OBSERVATIONS AND REMOTE SENSING (JSTARS) in 2019, and IEEE TRANSACTIONS ON GEOSCIENCE AND REMOTE SENSING (TGRS) in 2022. He is the Associate Editor for IEEE TGRS and IEEE JSTARS, Guest Editor for *Remote Sensing*, and the Reviewer for more than 30 international famous academic journals.